Microstructure and charge trapping assessment in highly reactive mixed phase TiO$_2$ photocatalysts

V. Likodimos [a],*, A. Chrysi [a], M. Calamiotou [a], C. Fernández-Rodríguez [b], J.M. Doña-Rodríguez [b], D.D. Dionysiou [c], P. Falaras [d],*

[a] Department of Solid State Physics, Faculty of Physics, National and Kapodistrian University of Athens, Panepistimioupolis, GR-157 84 Athens, Greece
[b] CIDIA-FEAM Universidad de Las Palmas de Gran Canaria, Edificio del Parque Científico Tecnológico de la ULPGC, Campus de Tafira, 35017 Las Palmas de Gran Canaria, Spain
[c] Environmental Engineering and Science Program, University of Cincinnati, Cincinnati, OH 45221-0071, USA
[d] Institute of Nanoscience and Nanotechnology, NCSR Demokritos, 153 10, Agia Paraskevi Attikis, Athens, Greece

ARTICLE INFO

ABSTRACT

The structural-microstructural characteristics and interfacial charge transfer are key issues to the development of efficient mixed phase TiO$_2$ photocatalysts. In this work, the interplay of lattice deformation and microstrains as well as the identification of charge trapping sites and electron transfer were investigated for a series of nanostructured titania photocatalysts by X-ray powder diffraction analysis, Raman and electron paramagnetic resonance (EPR) spectroscopy. These mixed phase nanomaterials were selected as model sol-gel TiO$_2$ systems based on their exceptional photocatalytic performance over a wide range of hazardous water pollutants (including degradation/mineralization of phenol, 2,4-dichlorophenoxyacetic acid and imazalil) under UV light. Lattice contraction with respect to the bulk anatase together with anisotropic microstrains was identified for the smallest (11 nm) anatase nanoparticles. Both effects gradually relaxed with the increase of calcination temperature and the concomitant particle growth, with microstrains scaling linearly with the relative change of the c-axis lattice constant and the broadening of the main anatase Raman mode. The growth of anatase nanoparticles at 1023 K with minimal lattice deformation and microstrains resulted in the optimal photocatalytic efficiency, outperforming the benchmark Aeroxide® P25 catalyst. This mixed phase catalyst comprised also larger, though more strained, rutile nanocrystals than P25, and presented an additional deeper electron trapping lattice site according to light-induced EPR measurements. More importantly, electron transfer from rutile to anatase lattice traps was identified by EPR under visible light in the mixed phase photocatalyst. The improved crystal quality of the anatase nanocrystals combined with the enhanced charge separation in anatase/rutile interfaces is concluded crucial to the design of competent solar photocatalytic nanomaterials.

1. Introduction

Titanium dioxide (TiO$_2$, titania) photocatalysis has been attracting enormous interest as one of the most promising technologies for environmentally benign water and air purification [1] and more recently solar-to-chemical energy conversion applications including hydrogen and chemical fuels' production by photocatalytic water splitting and CO$_2$ reduction [2]. This unique potential for solar powered technologies has been the incentive to the development of TiO$_2$ nanomaterials with improved structural,

morphological and optoelectronic properties [3] that could effectively circumvent the two major drawbacks of titania photocatalysts, i.e. the low quantum efficiency of TiO$_2$ stemming from photogenerated electron-hole recombination [4] and the intrinsically weak solar light harvesting capacity of TiO$_2$ due to the wide band gap (3.0–3.2 eV) of titania's polymorphic phases [5].

A wealth of different strategies has been accordingly devised to alleviate these detrimental effects that impair titania's photocatalytic efficiency [6]. They can be broadly classified in two categories: those relying on "extrinsic" modifications of TiO$_2$, the most potent comprising anion doping[7,8] coupling with noble metal nanoparticles (plasmonic photocatalysis) [9] and heterostructuring with other narrow band gap semiconductors [10,11] or carbon nanomaterials [12,13], and those based on

* Corresponding authors.
E-mail addresses: vlikodimos@phys.uoa.gr (V. Likodimos), p.falaras@inn.demokritos.gr (P. Falaras).

"self-structural" modifications of TiO_2 [14] that mainly involve tailoring titania's structural and morphological characteristics, i.e. nanomaterials phase, crystallinity, texture, size and shape, activating synergistic interfacial effects between polymorphic TiO_2 phases [15], as well as surface [16,17] and facet [18] engineering. Marked progress has been thereby achieved in extending the photocatalytic activity of TiO_2 under visible light, especially by means of the former approaches [8,19], as well as surface "disorder" engineering [20], though, in most cases, at the expense of the overall photocatalytic efficiency under solar light [21,22]. In particular, introduction of defects by means of extrinsic/intrinsic or even surface doping may compromise the photocatalyst's reactivity and the associated process efficiency for solar light photocatalytic applications, for which unmodified TiO_2 photocatalysts may eventually outperform modified ones [23].

Among the different crystalline TiO_2 phases, anatase that is the thermodynamically stable titania polymorph below a certain nanoparticle size (ca. 14 nm) [24], is generally reported as the most photocatalytically active TiO_2 phase [25]. Nevertheless, it was only recently that direct experimental evidence was provided for the comparatively longer exciton lifetime and diffusion length of anatase compared to rutile that support its high photocatalytic activity [26,27]. However, recent comparative works on anatase, rutile and brookite photocatalysts have shown that if the variation in the O_2 adsorption capacity of the different catalysts is taken into account by using Ag^+ as electron scavenger, the intrinsic photocatalytic activity of TiO_2 for organic degradation in water increases with its sintering temperature, regardless of its polymorphic phase composition [28–30]. Diverse results have further been reported concerning the particle size effects on the photocatalytic activity of TiO_2 nanocrystals [31,32]. The activity depends critically on the interplay of surface area, lattice strain, and defect structure with the nanomaterials' crystallinity, controlled by the catalyst synthesis conditions and calcination temperature [28–36]. Allowing for the implications of the substrate-specific reactivity of TiO_2 photocatalysts [37,38], the structural properties of titania nanocatalysts, i.e. lattice deformation and microstrain [39] as well as the concomitant size and phase variations of their microstructure are key to the establishment of structure-activity relations and fine tuning of the materials composition for specific target applications.

Furthermore, in several cases mixed phase TiO_2 photocatalysts have been reported to exhibit substantially higher efficiency than their single phase analogues, the most prominent example offered by the benchmark Aeroxide® P25 (Evonik) nanopowder catalyst consisting of a mixture of anatase/rutile nanocrystals [40]. Based on thorough electron paramagnetic resonance (EPR) experiments [41,42], interfacial electron transfer from rutile, acting as "antenna" to visible light photons, to anatase lattice traps has been proposed for P25 leading to reduced electron-hole recombination and higher photocatalytic efficiency, contrary to the oppositely directed anatase-to-rutile electron flow (rutile "sink" model) originally predicted for the mixed phase system based on the higher energy position of the anatase conduction band relative to that of rutile [43]. Recently, the long standing controversy on the energy band alignment between the anatase and rutile phases has been revisited by theoretical and experimental investigations indicating that both conduction and valence band edges of rutile lie above those of anatase providing the driving force for direct electron flow from rutile to anatase [44–46]. However, besides interfacial charge transfer, thorough experiments on biphase anatase-rutile photocatalysts have shown that transfer of O_2 preferentially adsorbed on the smaller anatase nanoparticles to the larger and more crystalline rutile ones may also contribute to the synergistic effect for the mixed phase system [47]. These last developments have triggered intensive theoretical and experimental investigations on the interfacial structure of anatase/rutile heterojunctions and the

identification of charge trapping sites that would determine the corresponding band offsets and charge or even O_2 flow between titania nanocrystals and eventually allow judicious design and engineering of efficient photocatalysts based on mixed phase TiO_2 [48–52].

Recently, the synthesis of highly reactive TiO_2 photocatalysts has been reported by means of an efficient sol-gel method combined with the removal of larger aggregates, appropriate aeration, and calcination [53]. Optimization of these catalysts resulted in mixed phase (anatase/rutile) TiO_2 nanocatalysts with markedly improved photocatalytic efficiency for water detoxification degrading a wide range of organic pollutants, including phenolic compounds, pesticides, herbicides and azo-dyes [53–55], endocrine disrupting compounds (17β-estradiol and bisphenol A) [56,57], caffeine, and diphenhydramine [23,58], an important pharmaceutical water pollutant. In most cases, these TiO_2 nanomaterials outperformed commercially available titania photocatalysts, especially the benchmark P25 catalyst that finds widespread use in most practical photocatalytic applications. Furthermore, the optimal catalyst showed superior efficiency in pilot plant scale photocatalytic oxidation, mineralization and detoxification of real waters containing the herbicides 2,4-dichlorophenoxyacetic acid (2,4-D) and bentazon, as well as toxic intermediates, under solar light [59], making the corresponding titania nanomaterials very promising photocatalysts.

In this work, following a complete and systematic investigation, we confirmed the effect of the structural-microstructural properties as well as of charge trapping and transfer on the activity of the above highly performing sol-gel photocatalysts. By combining powder X-ray diffraction (XRD) Rietveld refinement including microstrain analysis model, Raman and light-induced electron paramagnetic resonance (EPR) spectroscopies to deeply characterize the titania nanomaterials, we achieved to determine the evolution of phase composition, size dependence of lattice parameters and microstrain of the titania nanoparticles as well as charge separation with calcination temperature and nanoparticle growth, providing additional data that justified their higher photocatalytic activity with respect to that of the benchmark Aeroxide® P25 mixed-phase photocatalyst, over several model pollutants.

2. Experimental

2.1. Materials

TiO_2 nanocatalysts with high anatase phase content and improved crystallinity were prepared by an optimized sol-gel method using citric acid followed by high temperature calcination [53]. Briefly, materials synthesis was carried out via sol–gel hydrolysis precipitation of titanium butoxide using ethanol and citric acid, followed by sieving (63 μm mesh) of the aged and dried gel precipitates for the removal of the larger aggregates prior to their calcination at various temperatures. The corresponding catalysts are designated as "ECT" (ethanol, citric, tetrabutoxide) followed by the calcination temperature (in K) and the letter "t" for those that have been sieved. The samples ECT-673t, ECT-873t and ECT-1023t with specific surface areas (S_{BET}) of 63, 28 and 18 m^2/g, and optical absorption edges at 3.20, 3.19 and 2.97 eV, respectively, have been selected for the present work, in comparison with the standard mixed phase Evonik Aeroxide® P25 nanopowder (52 m^2/g).

2.2. Methods

X-ray powder diffraction measurements were performed on a Siemens D5000 powder diffractometer with Cu *K*a radiation and a graphite secondary monochromator at room temperature.
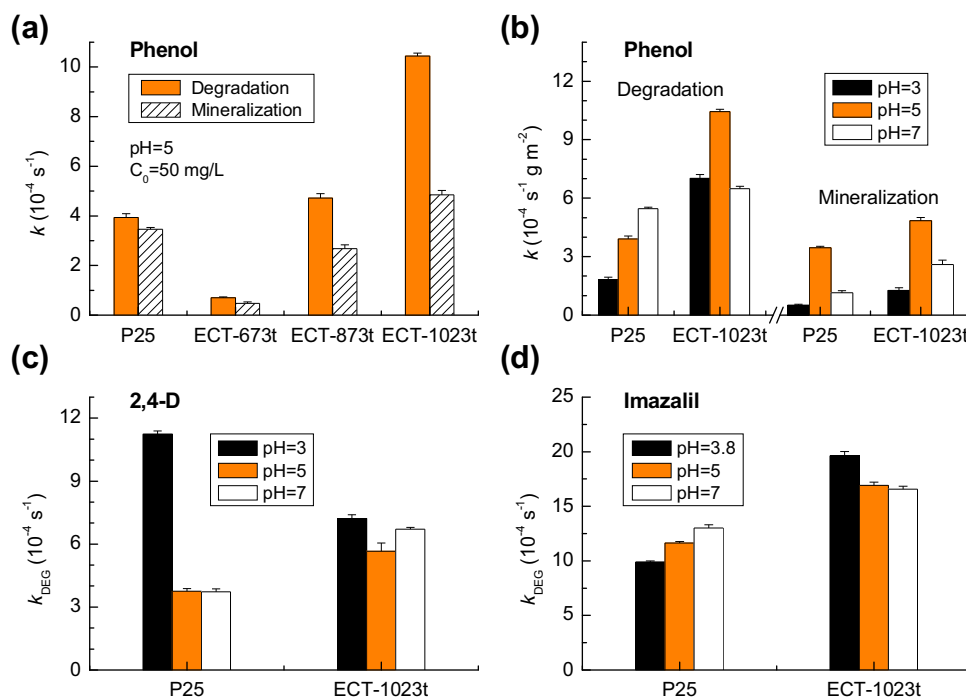
Fig. 1. (a) Apparent first order kinetic constants for phenol degradation (k_{DEG}) and mineralization (k_{MIN}) for the ECT photocatalysts compared to P25, under UV light. Apparent first order degradation kinetic constants (k_{DEG}) for (b) phenol (k_{MIN} is included), (c) 2,4-D (c) and (d) imazalil at different initial pH values for ECT-1023t compared to P25.

The XRD patterns were acquired in the standard Bragg-Brentano geometry by step scanning mode with a step size of 0.03° and a counting time of 6 s/step. The instrumental resolution function of the diffractometer and its contribution to line broadening was determined by a standard LaB_6 (NIST) sample. The structural and microstructural parameters of the titania samples were initially estimated by Le Bail fitting in combination with Williamson-Hall (WH) plots and then they were independently refined by Rietveld analysis using the FULLPROF suite including anisotropic microstrain and size peak broadening refinement [60]. In all cases, line profile analysis was performed using the Thompson-Cox-Hasting pseudo-Voight convoluted with axial divergence asymmetry function. For all refinements, atomic displacement parameters were fixed at the values reported for bulk anatase [61,62]. Micro-Raman spectra were measured in backscattering configuration on a Renishaw inVia Reflex microscope using an Ar$^+$ ion laser ($\lambda = 514.5$ nm) as excitation source. The laser beam was focused onto the samples by means of a 5× objective, while the laser power density was kept at low levels (<0.02 mW/μm^2) to avoid local heating.

EPR measurements were performed using an upgraded X-band ($\nu \approx 9.42$ GHz) Bruker ER-200D spectrometer with a rectangular 4102ST cavity in the TE102 mode, interfaced with a personal computer running appropriate software in the LabView programming environment and equipped with an Oxford ESR 900 cryostat, an Anritsu MF76A frequency counter, and a Bruker 035 M NMR gaussmeter [63]. Independent calibration measurements were performed using DPPH (α,α'-diphenyl-β-picryl hydrazyl). The signal-channel unit was replaced with an SR830 digital lock-in amplifier by Stanford Research. The powder samples of the same mass (~5 mg) were filled at the same level in quartz tubes (O.D. 4 mm) and cooled at 10 K, where continuous UV/Vis illumination by white light and simultaneous spectrum acquisition were directly (in situ) performed in the EPR cavity using a 360 W halogen lamp delivering ca. 4 mW/cm^2 equipped with a water filter to remove IR radiation. Alternatively, visible light illumination was implemented in the EPR cavity using a Luxeon light emitting diode (LED), which emits at the narrow royal blue spectral region

with maximum at 445 nm, full-width at half-maximum (FWHM) of approximately 20 nm and cutoff at about 420 nm with power density of ca. 0.5 mW/cm^2. No special treatment was applied to the samples prior to the measurements, i.e. the samples were kept and handled in the ambient laboratory environment under indoor light conditions. The EPR spectra were typically recorded at microwave frequency of ~9.42 GHz and modulation amplitude of 4 Gpp at 100 kHz, by averaging 5–10 scans to increase the signal-to-noise ratio with microwave power of 20 mW.

2.3. Photocatalytic performance

Photocatalytic experiments were performed with three different pollutants (phenol, 2,4-dichlorophenoxyacetic acid (2,4-D) and imazalil) under UV light. 2,4-D (pKa = 2.73) and imazalil (pKa = 5.85–6.5) were selected as model pollutants because of their markedly different acid-basic properties. All irradiation experiments were carried out in a 250 cm^3 Pyrex cylindrical reactor at 298 K. The initial concentration of the pollutants (C_0) was 50 mg L^{-1}, the catalyst load was 1 g L^{-1} and the reaction solution volume in the reactor was 200 mL. The solution pH was adjusted to 3 (3.8 for imazalil), 5 and 7. Sulphuric acid or sodium hydroxide were used to fix pH to the aforementioned values. Adsorption of organic compounds on the catalyst surface was favored by stirring and air-bubbling (400 mL min^{-1}) for 30 min in the dark before UV radiation or solar light exposure. A 60 W Solarium Philips HB175 equipped with four 15 W Philips CLEO fluorescent tubes with emission spectrum from 300 to 400 nm (maximum around 365 nm) and an incident irradiance of 90 W m^{-2} was used as UV light source.

The remaining phenol, 2,4-D and imazalil concentrations at different reaction times were HPLC-measured using a Supelco Discovery C18 25 cm × 4.6 mm ID, 5 μm particle column and an acetonitrile-water solution as mobile phase (20:80, v:v), using a Diode Array Detector (DAD) ($\lambda = 270$ nm) for analysis of phenol, an acetonitrile-10 mM KH_2PO_4 solution (45:55) with 100 mg/L of sodium 1-octanesulfonate as mobile phase (adjusted to pH 3.0 with phosphoric acid) and ($\lambda = 225$ nm) for imazalil analysis and a

methanol-25 mM phosphate buffer pH 2.3 aqueous solution (70:30, v:v) as mobile phase and λ = 214 nm for 2,4-D analysis. The extent of mineralization was determined using a total organic carbon (TOC) analyzer (TOC-VCSH, Shimadzu). Photocatalytic degradation of all three compounds followed pseudo-first-order kinetics and, thus, the apparent reaction rate constants k were determined from the slope of the plot $\ln(C/C_0)$ vs. reaction time in units of $[s^{-1}]$. The photocatalytic experiments were performed three times for each pollutant and pH value under identical conditions. The standard deviations of the average k values are reported as error bars in Fig. 1 and were always below 6%, indicating the very good reproducibility of the photocatalytic evaluation.

3. Results and discussion

3.1. Photocatalytic activity

Fig. 1(a) summarizes the results on phenol photocatalytic degradation (k_{DEG}) and mineralization (k_{MIN}) kinetic constants for the ECT TiO$_2$ and P25 samples under UV light. Fig. 1(b)–(d) show the effect of the solution pH value on the photocatalytic degradation constants for the three different pollutants under UV light. For the ECT series, the photocatalytic degradation kinetics strongly depended on the TiO$_2$ particle size. By increasing particle size, significantly higher kinetic constant values were obtained, with ECT-1023t presenting the highest degradation and mineralization kinetic constant. In addition, ECT-1023t outperformed P25 in the photocatalytic degradation of all model pollutants, verifying its high photocatalytic reactivity except for 2,4-D at pH 3 (Fig. 1). However, a previous study has shown that the photocatalytic degradation of 2,4-D by P25 depends strongly on the pollutant's adsorption on the catalyst surface [55]. The amount of 2,4-D adsorbed on P25 was 11.1 μmol g^{-1} at pH 3, 5.83 μmol g^{-1} at pH 5 and negligible at pH 7. The photocatalytic degradation constant is highest at pH 3, where the pollutant adsorption on this semiconductor is greatly favored. On the other hand, pollutant adsorption was not found to be an important parameter for ECT-1023t (3.43 μmol at pH 3 and negligible at pH 5 and 7) that presented nearly pH independent k_{DEG} values for 2,4-D photodegradation (Fig. 1). In that case, normalization of the degradation and mineralization kinetic constants to the catalysts' specific surface area (S$_{BET}$) resulted in a marked rise of ECT-1023t photocatalytic activity compared to that of P25; ECT-1023t presented seven and four-fold higher normalized k_{DEG} and k_{MIN} kinetic constants than those of P25, as shown in Fig. S1 (Supplementary material). The photodegradation mechanism of 2,4-D by P25 at pH 3 occurs mainly by direct oxidation through photogenerated holes. However, the enhanced photoactivity of ECT-1023t at pH where adsorption is negligible indicated that the primary oxidative species in this catalyst are free hydroxyl radicals. In fact, ECT-1023t produces more free •OH than P25 as was previously proved using isopropanol as hydroxyl radical scavenger [64].

In the case of imazalil, the amount of compound adsorbed on P25 at pH value of 3.8, 5 and 7 was 28.5, 145.2 and 216.1 μmol g^{-1}, respectively. The photodegradation rate of this compound with P25 also rose as adsorption increased. On the contrary, ECT-1023t showed the highest photocatalytic activity at pH values not favoring the adsorption of this basic compound. The increased efficiency of ECT-1023t with regard to P25 at pH 5 or 7 occurs even though fewer molecules are adsorbed on the catalyst, 125 μmol g^{-1} at pH 5 and 115 μmol g^{-1} at pH 7, respectively. This result also proves that ECT-1023t produces more reactive radicals than P25. A detailed study of the structural parameters and charge separation of the ECT series compared to P25 is presented below in order to unveil
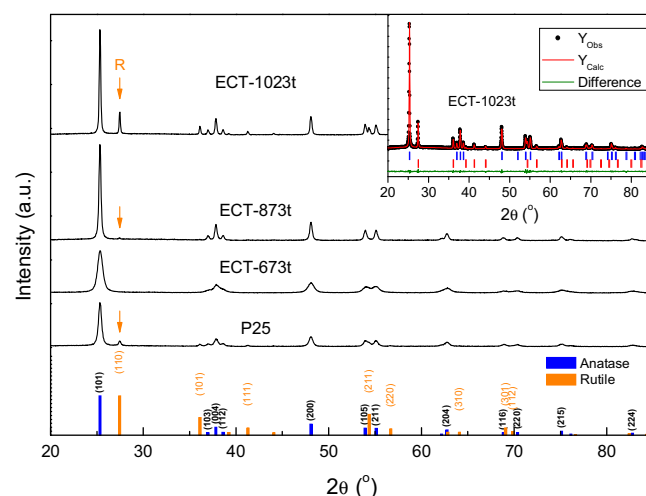

Fig. 2. XRD patterns of the ECT samples calcined at different temperatures in comparison with P25 and the prototype powder diffraction patterns of anatase (ICPDF #01-089-4921) and rutile (ICPDF #00-002-0494). The inset shows the Rietveld fit to the experimental data for ECT-1023t.

the differences that justify the enhanced photoactivity of the ECT sample calcined at 1023 K.

3.2. Structural and microstructural parameters

Fig. 2 shows the XRD spectra of the different ECT samples in comparison with P25. Increase of the calcination temperature resulted in the sharpening of the XRD peaks, indicative of the growth of the titania nanoparticles. Rietveld refinement of the powder diffraction patterns (inset of Fig. 2) revealed that ECT-673t is single phase anatase TiO$_2$ (space group $I4_1/amd$), while minute amount of a secondary rutile phase (space group $P4_2/mnm$) was traced for ECT-873t after calcination at 873 K. Further increase of the calcination temperature at 1023 K (ECT-1023t) resulted in the growth of titania crystallites along with the increase of the rutile phase content. Table 1 summarizes the structural parameters derived by Rietveld refinement for the anatase and rutile phases in the ECT and P25 samples. The corresponding microstructural parameters, i.e. the average maximum micro○strains ε and the volume averaged size $\langle L \rangle$ of essentially spherical [53], coherently diffracting domains, are also included. In the case of nanocrystalline materials, $\langle L \rangle$ can be directly related to the mean crystallite size. Standard deviations in average size and microstrains are calculated using the different reciprocal lattice directions and are therefore a measure of the degree of anisotropy.

Fig. 3 shows the evolution of the anatase c/a lattice ratio with the average size $\langle L \rangle$ for the different titania samples determined by Rietveld analysis. Continuous increase of the unit cell ratio toward the value of bulk anatase occurred with the increase in calcination temperature and the concurrent particle growth, stemming mainly from the elongation of the c-axis and, to a lesser extent, the small shortening of the a-axis (inset of Fig. 3). This distinct size dependence of the c-axis together with a relatively weaker variation (decrease or increase) of the a-axis has been amply identified in nanocrystalline anatase TiO$_2$ [65–72]. The development of negative or positive strain along the a and c-axes leading to lattice contraction or, less frequently, expansion of the unit cell relative to that of bulk anatase has been accordingly observed in TiO$_2$ nanoparticles. This behavior has been rationalized by the diverse variations of the surface free energy with particle size, surface ligands and hydration or even Ti vacancies (especially for particle sizes below 10 nm) and the accompanying effects on the surface stress that is exerted on the nanoparticle structure, as thoroughly reviewed by

Table 1
Structural and microstructural parameters for the anatase and rutile nanocrystals derived from Rietveld analysis for the ECT and P25 samples.

	P25	ECT-673t	ECT-873t	ECT-1023t		P25	ECT-873t	ECT-1023t
		Anatase					Rutile	
⟨L⟩ (nm)	24.6(0)[a]	11(0)	36.7(0)	51.4(0)	⟨L⟩ (nm)	26.4(0)	22.9(0)	82.8(0)
ε (×10^4)	30.5(7)	50(2)	19.8 (0)	14 (2)	ε (×10^4)	18.2(0)	11(6)	18(5)
Fraction (wt%)	90.4	100	98.7	82.4	Fraction (wt%)	9.6	1.3	17.6
a (Å)	3.7845(1)	3.7859(1)	3.7839(1)	3.7837 (1)	a (Å)	4.5922(3)	4.587 (7)	4.5917(2)
c (Å)	9.5030(4)	9.4977(4)	9.5082(3)	9.5097(2)	c (Å)	2.9587(4)	2.951(6)	2.9577 2)
V (Å)^3	136.11(1)	136.12(1)	136.14(1)	136.14(1)	V (Å)^3	62.39(1)	62.47(0)	62.36(1)
Ti (4b)	(0,1/4,3/8)	(0,1/4,3/8)	(0,1/4,3/8)	(0,1/4,3/8)	Ti (2a)	(0,0,0)	(0,0,0)	(0,0,0)
O (8e) (0,1/4,z)	0.5809(3)	0.5807(3)	0.5810(0)	0.5814(0)	O (4f) (x,x,0)	0.307(3)	0.307(0)	0.311(0)

[a] (esd) are calculated using the different reciprocal lattice directions and thus represent the corresponding anisotropies.
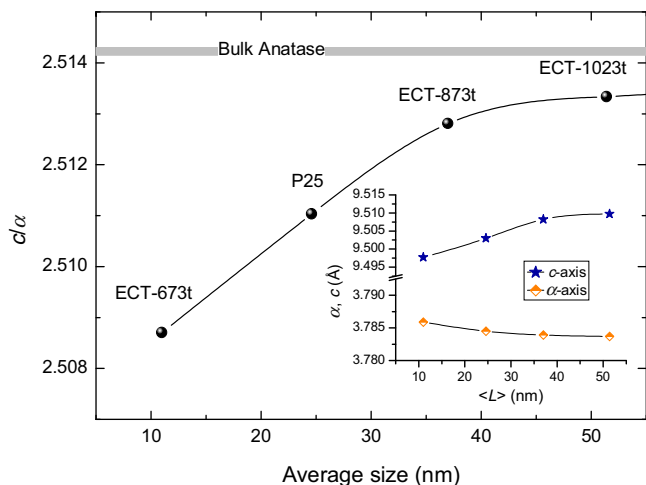
Fig. 3. Size dependence of the *c/a* ratio for the anatase phase of ECT and P25. The inset shows the corresponding variation of *a* and *c* lattice parameters. The grey shaded line depicts the corresponding ratio for bulk anatase, while solid lines are guides to the eye.
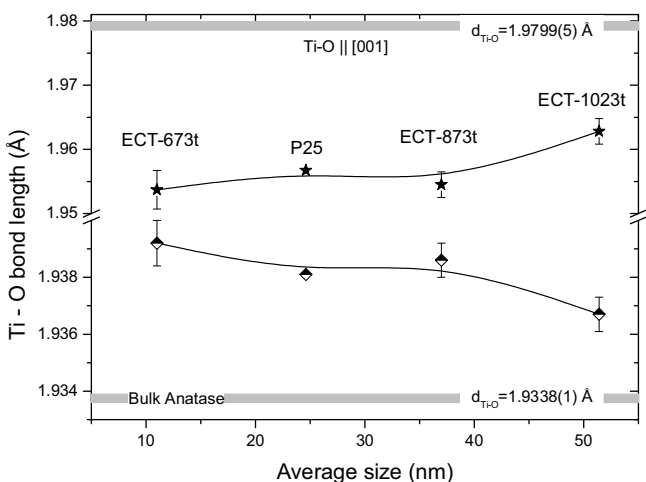
Fig. 4. Size dependence of the long (|| [001]) and short Ti-O bond lengths of the TiO$_6$ octahedra for the anatase ECT and P25 nanoparticles. Grey shaded regions depict the corresponding values for bulk anatase [73]. Solid lines are guides to the eye.

Zhang and Banfield [39]. In the present case, the long (along the *c*-axis) and short Ti—O bond lengths of the TiO$_6$ octahedra [73] were found to increase and decrease, respectively, as the average size of the anatase nanoparticles increased, leading to the relaxation of lattice deformation with respect to the bulk structure, as shown in Fig. 4. The relative variation of the two elongated apical Ti—O bonds (along [001]) was distinctly higher (ca. −1.2%) than that of the four

equatorial short Ti—O bonds (ca. +0.2%), reflecting the high compressibility of the anatase lattice along the *c*-axis [74], induced by the strong repulsion between Ti^{4+} ions across the four shared edges of the TiO$_2$ octahedra [69]. The ECT unit cell volume was accordingly found to decrease slightly with the decrease of the average size of the anatase nanoparticles (Table 1), while the relative volume change $\Delta V/V_0$ with respect to the bulk anatase value (V_0) varied around −0.1%, signifying the concomitant lattice contraction of the ECT nanocrystals [70]. Refinement of the site occupation factor for titanium in the Rietveld analysis, in addition to the structural and profile parameters, resulted in the identification of Ti deficiency only for the ECT-673t sample (Ti occupancy ∼98%), in close agreement with previous results on sol-gel TiO$_2$ nanoparticles of 10 nm size [69]. On the other hand, varying the Ti occupancy parameter during Rietveld refinement for all the other samples, did not improve the agreement factors, i.e., R$_f$ and R$_{wp}$, and thus the Ti occupancy was kept constant to 100%.

Moreover, the relative volume change, $\Delta V/V_0$, for the rutile nanoparticles of ECT-1023t (−0.121%) was approximately double the corresponding one of P25 (−0.065%). The persistence of higher lattice strain for the ECT-1023t rutile particles than those of P25 could be thus concluded, despite the significantly larger rutile crystallites, 83 nm, for ECT-1023t compared with 26 nm for P25 (Table 1). This would further suggest that is not merely the particle size that controls the change of the lattice parameters and the associated lattice deformation but also the specific phase stability of nanocrystalline TiO$_2$ [39] with respect to the preparation process and the calcination temperature [29]. In fact, while the lattice parameters for the P25 anatase nanoparticles interpolate nicely between the ECT ones according to their size (Fig. 3), the rutile particles of P25 are considerably less strained than those of ECT-1023t, albeit their much smaller size. This could be related to the different preparation method of the two materials, i.e. sol-gel hydrolysis precipitation followed by thermal calcination for ECT-1023t vs flame hydrolysis of titanium tetrachloride at higher temperatures (1273–2673 K) for P25 (AEROSIL® process) [75] that seems to be most effective in reducing lattice strain for the rutile phase.

A first assessment of the ECT nanoparticles' microstructure has been performed using the Williamson-Hall method providing a simple, semi-quantitative means for the separation of size and microstrain effects on the integral breadth of the diffraction peaks [76]. Assuming that the particle size and microstrains contributions to line broadening are independent to each other and both have a Lorentzian profile (Cauchy approximation), the corresponding integral breadths are linearly additive to obtain the total integral breadth β, after subtraction of the instrumental broadening, as

$$\beta \frac{\cos\theta}{\lambda} = \frac{1}{\langle L \rangle_V} + 4\varepsilon \frac{\sin\theta}{\lambda},$$

where $\langle L \rangle_V$ is the volume-weighted average crystallite size and ε is the average maximum (upper limit) microstrain. In the case of

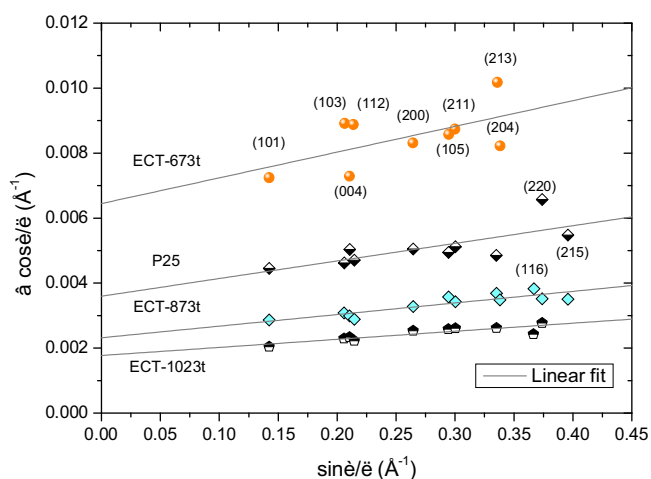**Fig. 5.** Williamson-Hall plots for the anatase ECT and P25 nanoparticles. Solid lines correspond to the linear best fit curves.

Fig. 6. Size dependence of microstrains for the anatase ECT and P25 nanocrystals. The dashed line corresponds to the best fit to a power law $\propto 1/\langle L \rangle^a$ with $a = -0.8(1)$. Standard deviations (shown as error bars) represent the degree of anisotropy. The inset shows the linear variation of microstrains with the relative change of the c-axis $|\Delta c/c_0|$.

isotropic microstrains broadening, a plot of the integral breadth in reciprocal space $\beta \cos\theta/\lambda$ vs. $\sin\theta/\lambda$ (W-H plot) should result in a straight line, whose intercept at the origin gives the crystallite size $\langle L \rangle_V$ and its slope allows determining the maximum microstrain $\varepsilon = \Delta d/d_0$, where Δd represents the width of the distribution of interplanar spacing from the average value d_0. Fig. 5 shows the W-H plots for the anatase diffraction patterns of ECT and P25 fitted by the Le Bail method, where (hkl) peaks, whose width could not be accurately determined due to overlapping or low intensity, were not included. A gradual increase of the crystallite size together with the decrease of microstrains was thus derived with the increase of the calcination temperature, in agreement with previous reports on nanocrystalline anatase [34,35,66,71]. However, in contrast to ECT-1023t and ECT-873t, the W-H plot for ECT-673t deviated significantly from linearity, indicative of the development of anisotropic microstrains for the smallest anatase nanoparticles, which relaxed with the particle growth. The corresponding W-H plots for the rutile nanoparticles of ECT-1023t and P25 obtained by the diffraction peaks, whose width could be reliably fitted, indicated crystallite sizes of 83 and 37 nm, respectively (Fig. S2 in Supplementary material), consistent with the Rietveld analysis. On the other hand, the slopes of the W-H plots were similar for ECT1023t and P25, implying comparable microstrains maxima. However, the rutile ECT-1023t W-H plots presented appreciable scatter of the data points, indicative of larger microstrain anisotropy. This behavior together with the increased static lattice strain derived for the ECT-1023t rutile nanoparticles from the corresponding lattice constants (Table 1), corroborates the influence of the synthesis method on rutile's crystallinity.

Microstrains were accurately determined by Rietveld refinement with the incorporated anisotropic microstrain model in FULLPROF for both the anatase and rutile phase of ECT and P25 samples (Table 1). Fig. 6 displays the dependence of the upper limit of microstrains on the anatase nanoparticle size that follows semi-quantitatively the results of the W-H plot analysis and most importantly correlates directly with the improved photocatalytic activity of the materials (Fig. 1). Furthermore, microstrains vary linearly with the relative change of the lattice parameters that cause lattice deformation, especially that of the c-axis (inset of Fig. 6). This common size dependence verifies that microstrains and lattice deformation, reflected in the broadening and shift of the diffraction peaks, respectively, are intrinsically connected for anatase nanoparticles [66], similar to other nanocrystalline systems [77]. It can be accordingly inferred that the size dependent surface stress that emerges at the highly distorted shell of anatase
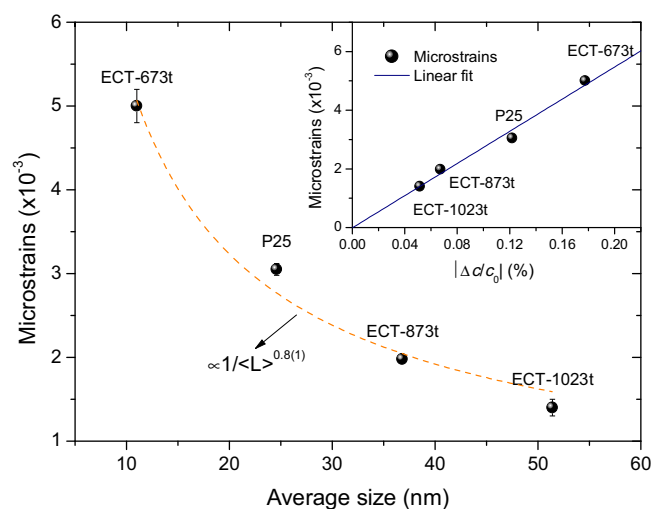
nanoparticles will generate both local strains leading to anisotropic microstrains as well as changes of the unit cell parameters resulting in lattice deformation with respect to the bulk material. In particular, fitting the size dependence of both microstrains and the relative change of the c-axis lattice parameter $\Delta c/c_0$ to a power law of the form $\propto 1/\langle L \rangle^a$ leads to the exponent value $a = 0.8(1)$, in perfect agreement to that previously determined by Djerdj and Tonejc for nanocrystalline anatase with sizes in the range of 4–14 nm [66]. Thereby, ε scales linearly with $|\Delta c/c_0|$ with no residual microstrains at $|\Delta c/c_0| = 0$ (inset of Fig. 6), indicating that the underlying lattice compression at small sizes determines microstrains in the anatase nanoparticles, as well. The suppression of microstrains and lattice deformation for the ECT-1023t anatase nanocrystals suggests that the concentration of dislocations or other crystal defects [39], would be greatly reduced leading to improved crystal quality of the material. This is particularly important for the reduction of the electron-hole recombination in the anatase nanoparticles that is the major phase of ECT-1023t. Fig. 7 shows the corresponding evolution of phenol's degradation kinetic constants as a function of both anatase lattice deformation quantified by $\Delta c/c_0$ as well as ε for the different samples. A marked increase of k_{DEG} with the decrease of lattice deformation and microstrains could be thus evinced, demonstrating the close correlation of anatase's structural − microstructural parameters with the materials photocatalytic activity. On the other hand, the ECT-1023t rutile nanocrystals presented similar ε values, i.e. the upper limit of average microstrains, to P25 (Table 1). However, the corresponding standard deviation was appreciably higher for ECT-1023t, indicating the presence of larger microstrain anisotropy, in agreement with the W-H analysis. This variation supports the significant role of preparation conditions on rutile's structural characteristics.

The structural characteristics and phase composition of the ECT photocatalysts were further investigated by Raman spectroscopy. Fig. 8 displays the Raman spectra of ECT-673t, ECT-873t and ECT-1023t in comparison with P25 at 514.5 nm. The ECT-673t and ECT-873t samples exhibit the characteristic Raman-active phonons of the anatase TiO$_2$ phase, at approximately 144 (E_g), 197 (E_g), 396 (B_{1g}), 516 ($A_{1g} + B_{1g}$), and 638 cm^{-1} (E_g) as well as two rather weak and broad bands at about 320 and 795 cm^{-1}, which can be attributed to disorder-induced scattering and the first overtone of the lowest B_{1g} mode, respectively [78]. Further increase of the cal-
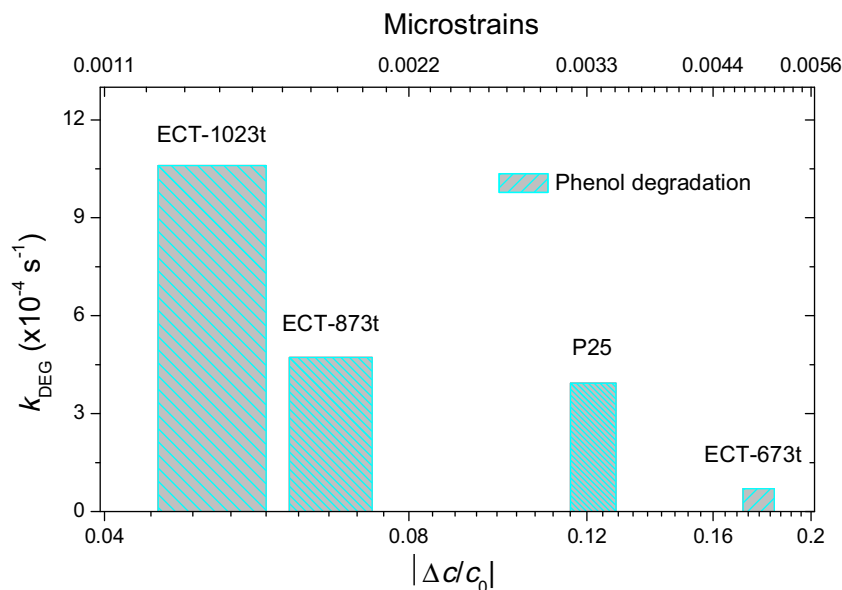
Fig. 7. First order phenol degradation kinetic constants k_{DEG} as a function of the relative change of the c-axis $|\Delta c/c_0|$ and microstrains for the anatase phase of ECT photocatalysts and P25.
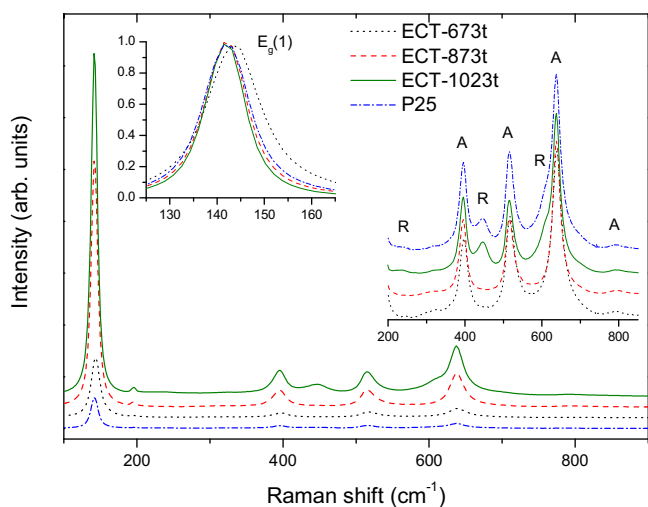

Fig. 8. Raman spectra of ECT and P25 samples at 514.5 nm. The left and right insets compare in detail the Raman spectra after normalization to the intensity of the lowest frequency anatase $E_g(1)$ mode.

cination temperature for ECT-1023t, resulted in the growth of the rutile phase, readily identified by the most intense rutile Raman modes at ~445 (E_g) and 610 cm^{-1} (A_{1g}), as shown in the right inset of Fig. 8. This variation is in perfect agreement with the corresponding XRD results, where the rutile phase could be traced only for the ECT samples calcined at higher temperatures (T ≥ 873 K). Spectral analysis showed that the relative anatase/rutile I(A_{395})/I(R_{445}) intensity ratio, determined from the integrated areas of the anatase 396 cm^{-1} and rutile 445 cm^{-1} bands, attained values of 2.6 and 3.5 for the ECT-1023t and P25 samples, respectively. According to the calibration data derived by Raman measurements at 532 nm for mechanical mixtures of anatase and rutile nanoparticles [79], these values indicate anatase-rutile weight ratios of approximately 8 (89% anatase-11% rutile) and 11 (ca. 92% anatase-8% rutile) for ECT-1023t and P25, respectively. While the latter value is close to the phase composition of the P25 sample determined by XRD (Table 1), the anatase phase content for ECT-1023t is quite overestimated.

Although the latter difference may be reasonable given the approximations involved, it is most likely associated with the variation of the scattering efficiency of the TiO$_2$ nanoparticles, whose Raman intensity can be enhanced to a different extent for the anatase and rutile crystallites, as they grow in size for ECT-1023t.

In fact, upon increasing the calcination temperature a marked intensity enhancement of the anatase Raman bands was systematically observed for all the ECT samples, concomitantly with the increase of the crystallite size (Fig. 8). This was particularly pronounced between ECT-673t and ECT-873t, where a fourfold increase of the lowest $E_g(1)$ anatase mode was detected, following closely the relatively large (threefold) increase of the anatase crystallite size. Moreover, analysis of the latter mode revealed appreciable frequency shift only for the sample with the smallest anatase crystallites, i.e. ECT-673t, as shown in Fig. S3 (Supplementary material), where the evolution of peak position and full-width at half-maximum (FWHM) of the $E_g(1)$ mode with the anatase crystallite size is depicted. This behavior can be explained by the gradual release of size effects stemming from optical phonon confinement that result in the asymmetric broadening and shift of the Raman modes due to the relaxation the $k = 0$ selection rule for nanosized materials [80,81]. As the anatase crystallite size grows appreciably above 20 nm, phonon confinement effects are practically suppressed precluding any shift of the $E_g(1)$ mode, as evidenced for ECT-873t and ECT-1023t (left inset of Fig. 8). However, the width of the $E_g(1)$ mode exhibited a weak but continuous decrease with the increase of the crystallite size up to ECT-1023t that could not be accounted for by phonon confinement at such large crystallite sizes. Instead, this size dependence scaled linearly with microstrains in the anatase ECT and P25 nanocrystals, as shown in the inset of Fig. S3. Furthermore, despite its sensitivity to lattice compression [74], the frequency of the $E_g(1)$ mode that stems from the O—Ti—O bond bending vibrations in the TiO$_6$ octahedra was practically constant for the ECT-873t, ECT-1023t and P25 samples and thus hardly affected by lattice deformation of the anatase phase. The $E_g(1)$ mode narrowing and intensity enhancement with the calcination temperature can be accordingly related to the relaxation of microstrains and the increased scattering efficiency of the anatase nanoparticles, respectively, both reflecting the improved crystallinity of the ECT materials.
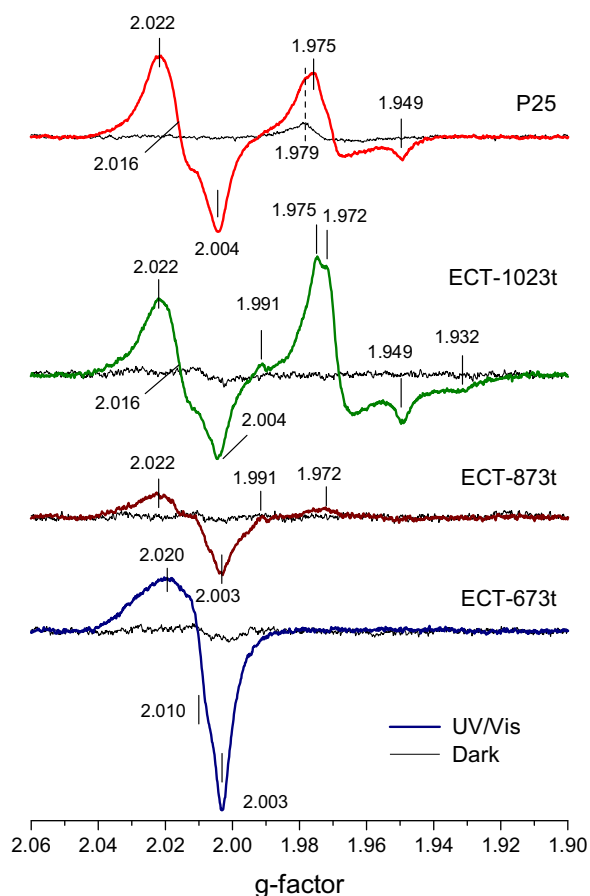
Fig. 9. EPR spectra of ECT and P25 under dark (thin lines) and UV/Vis illumination (thick lines) at $T = 10$ K. EPR conditions: microwave frequency 9.425 GHz, modulation frequency 100 KHz, modulation amplitude 4 Gpp, microwave power 20 mW, and temperature 10 K.

3.3. Charge trapping and electron transfer

Charge trapping in the ECT photocatalysts was investigated by means of EPR spectroscopy under UV/Vis illumination at low temperatures. Fig. 9 compares the EPR spectra of ECT-673t, ECT-873t, ECT-1023t and P25 before (dark) and after UV/Vis illumination at 10 K. Under dark conditions, no appreciable EPR signal could be detected for the ECT samples, indicating the absence of any intrinsic paramagnetic centers. Upon UV/Vis illumination, ECT-673t exhibited a broad EPR powder spectrum of rhombic-like symmetry with g-values of $g_x = 2.003$, $g_y \sim 2.010$ and $g_z = 2.020$. This type of EPR spectrum is characteristic of photo-generated oxygen radicals such as O^- arising from trapped holes at O^{2-} ions, and superoxide anions (O_2^-) that form upon trapping of photo-generated electrons by O_2 molecules adsorbed on TiO_2 [82,83]. Although poorly resolved, the observed g-values indicate that the main contribution to the EPR spectrum stems from superoxide anions, where the rather broad width of the g_z component (low field side) implies a wide spread of the corresponding g_z-values and thus a broad distribution of the underlying O_2^- species [84,85]. On the other hand, no EPR signal was observed at $g < 2.00$, where the EPR spectra of localized Ti^{3+} ions originating from trapped electrons at lattice or surface Ti^{4+} sites, are expected [82]. This implies that most of the photo-generated electrons during illumination become scavenged by molecular O_2 for ECT-673t and/or remain delocalized in the anatase conduction band [84–86]. A similar, though less intense, EPR signal due to oxygen radicals was observed for ECT-873t, implying a decrease of the concentration of surface sites for O_2 adsorption on the anatase

nanoparticles upon calcination at higher temperatures. In addition, two very weak EPR signals could be barely traced at $g = 1.991$ and $g = 1.972$, corresponding closely to the perpendicular $g_\perp$ components of the axial Ti^{3+} EPR spectra that form via electron trapping in the anatase and rutile lattice, respectively [82,87]. The latter EPR signal verifies that rutile growth initiated already at 873 K for ECT-873t, as evidenced by XRD. Moreover, the very weak intensity of the Ti^{3+} EPR signals indicates the formation of a relatively low number of lattice electron traps, as the anatase crystallite size increased for ECT-873t.

Further increase of the crystallite size for ECT-1023t, resulted in a marked enhancement of localized Ti^{3+} and oxygen related EPR signals, resembling closely the EPR spectra of P25 that disposes a similar mixed (anatase/rutile) phase composition to ECT-1023t. Specifically, P25 exhibited an axial EPR powder spectrum at the higher field region ($g < 2.0$) with $g_\perp = 1.975$ and $g_\parallel = 1.949$, typical of trapped electrons at Ti^{4+} lattice sites in the rutile nanoparticles [41]. A very weak shoulder was also traced at $g = 1.979$, which can be most clearly identified in the P25 EPR spectra before illumination. This distinct EPR signal has been assigned to trapped electrons at tetrahedral Ti^{4+} sites at the anatase-rutile interfaces in P25, promoting charge transfer between the two TiO_2 polymorphs and underlying the unique photocatalytic activity of P25 [42,88], though more recent work suggested that interfacial defects may instead act as recombination centers [36].

An intense anisotropic EPR powder spectrum with rhombic g-tensor ($g_x = 2.004$, $g_y = 2.016$ and $g_z = 2.022$) was further observed at $g > 2.0$ for P25, which may comprise the contribution of both trapped holes (O^-) and superoxide anions (O_2^-) on the anatase/rutile particle surfaces [82,83,88]. Similar oxygen radical EPR spectrum was observed for ECT-1023t, suggesting that it is characteristic of the mixed anatase/rutile phase. Moreover, ECT-1023t presented the characteristic axial Ti^{3+} EPR spectrum of trapped electrons at the rutile lattice ($g_\perp = 1.975$ and $g_\parallel = 1.949$), similar to P25. In addition, the perpendicular ($g_\perp$) component of the EPR signal of trapped electrons in the anatase lattice was clearly resolved at $g_\perp = 1.991$ [82,83], while there was no trace of the interfacial $g = 1.979$ EPR signal, which may be either absent or even masked by the intense rutile $g_\perp$ line. Furthermore, two additional EPR lines were observed at $g = 1.972$ and $g = 1.932$, which can be assigned to the perpendicular $g_\perp$ and parallel $g_\parallel$ components of an axial Ti^{3+} EPR spectrum, respectively, present only in ECT-1023t. These EPR lines were relatively sharp with g-values close to those of rutile lattice Ti^{3+} sites rather than those of anatase [87]. This indicates that the latter EPR spectrum can be associated with a new electron trapping lattice site that emerges on the rutile nanoparticles of ECT-1023t. The latter should consequently comprise a higher density of point defects compared to the smaller rutile nanoparticles of P25, which supplements the higher static strain and microstrain anisotropy derived from the Rietveld structural refinement of ECT-1023t (Table 1). This would further support the influence of the preparation method on the crystallinity of rutile particles in mixed-phase TiO_2 systems. In addition, accurate simulation of the EPR powder spectra could provide valuable information on the relative concentration of trapped electrons and holes in the anatase or rutile nanocrystals [89]. However, the poor resolution of the observed X-band EPR spectra due to the severe overlap of the different signals largely precludes precise spectral deconvolution, which would require high field EPR measurements for a reliable simulation analysis and quantification of the underlying paramagnetic centers.

In order to further explore charge separation and the possibility of electron transfer between the anatase and rutile phases in ECT-1023t, additional EPR experiments were conducted under visible light illumination provided by a royal blue LED source (445 nm) with cutoff of ~420 nm, at 10 K. Fig. 10 compares the
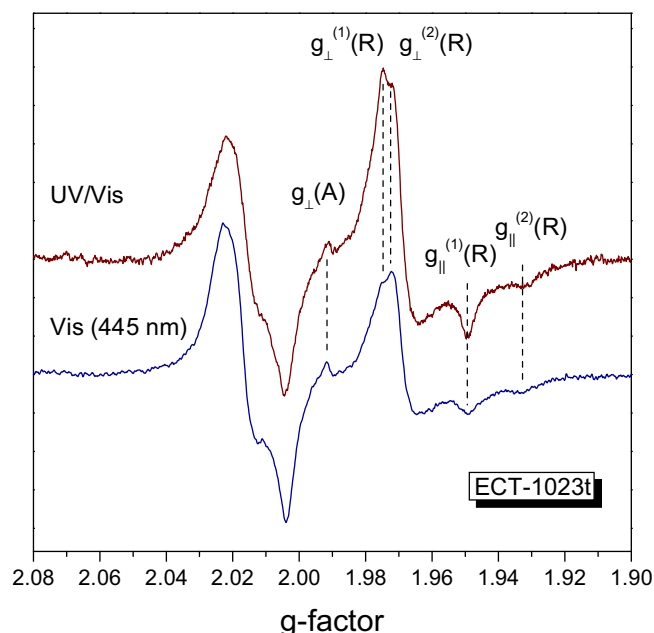
Fig. 10. EPR spectra of ECT-1023t under UV/Vis and visible light illumination at 10 K. EPR conditions: microwave frequency 9.425 GHz, modulation frequency 100 KHz, modulation amplitude 4 Gpp, microwave power 20 mW, and temperature 10 K.

corresponding EPR spectra of ECT-1023t obtained under UV/Vis and visible light. In that case, all the distinct EPR signals related to oxygen radicals and localized Ti^{3+} ions, comprising both the anatase $g_\perp(A)$ and the two rutile lattice trapping sites, depicted by $g^{(1)}$ and $g^{(2)}$ in Fig. 10, were excited in ECT-0123t by visible light. Although the excitation light energy is only near the rutile or even smaller than the anatase band gaps, the appearance of the photo-generated EPR spectra can be readily rationalized as the underlying electron trap states are predicted to lie ~0.8 eV below the bottom of titania's conduction band [90], rendering them accessible to near or sub-band gap illumination. However, comparison of the relative EPR intensity of the two rutile, $g_\perp^{(1)}(R)$ and $g_\perp^{(2)}(R)$, and the anatase, $g_\perp(A)$, electron trapping signals revealed appreciable differences between UV/Vis and visible light illumination. In particular, the intensity of the $g_\perp^{(2)}(R)$ component was appreciably enhanced compared to $g_\perp^{(1)}(R)$ under visible light, implying that the energy of the new trap state (2) is lower than (1), relative to the top of the rutile valence band. In that case, electron excitation is promoted in the deeper trap states (2) than (1) under the lower illumination energy provided by the LED source. Most importantly, the intensity of the anatase $g_\perp(A)$ electron trapping EPR signal was considerably increased with respect to those of the rutile traps, $g_\perp^{(1)}(R)$ and $g_\perp^{(2)}(R)$, under visible light. Specifically, the peak-to-peak height of the anatase $g_\perp(A)$ component relatively to the $g_\perp^{(1)}(R)$ and $g_\perp^{(2)}(R)$ ones increased approximately by a factor of two. This variation can be explained if we allow for the presence of electron transfer from the rutile to the anatase lattice trap states under visible light, similar to the original model proposed by Hurum et al. for charge transfer via trapping sites in P25 [41]. This was directly corroborated by the visible light induced EPR spectra of P25, as can be seen in Fig. S4 (Supplementary material). A weak though clear signal of the anatase $g_\perp(A)$ component could be observed in the P25 EPR spectra under visible light that could be hardly traced in the corresponding ones under UV/Vis light, confirming the rutile-to-anatase electron transfer.

Although the relatively large size of the anatase and rutile nanoparticles (Table 1) may lead to a relatively low density of anatase/rutile interfaces and thus partially hinder extensive charge

transfer for ECT-1023t, the relative decrease of the rutile EPR signals especially of the higher energy traps (1) indicates that a substantial fraction of trapped electrons in the rutile phase flows to anatase in the ECT-1023t aggregates, whose relatively large size (ca. 39 μm) also leads to faster sedimentation in solar photocatalytic applications, compared to the ~3 μm P25 aggregate particles [59]. The driving force for electron transfer from rutile to anatase under UV/vis illumination may be further promoted by the staggered alignment of their energy bands with the valence band maximum of rutile to be 0.4-0.7 eV higher than that of anatase [45,46] or even by the presence of O_2 as electron scavenger in the case of aligned conduction bands, as recently proposed by transient IR absorption-excitation spectra [52]. Furthermore, the higher H_2O_2 concentration detected when using ECT-1023t compared to P25 in the phenol degradation studies [53], may also corroborate the presence of additional rutile electron traps, which can produce an increased hydroxyl radical concentration by the reduction of H_2O_2 forming from adsorbed O_2. Hirakawa et al. studied the •OH production after the addition of H_2O_2, using mixed anatase-rutile TiO_2 suspensions of various proportions [91]. They observed that the •OH concentration increased only when rutile was present, indicating that the formation of •OH from H_2O_2 takes place mainly on the rutile phase. This fact could justify the increased photocatalytic activity of ECT-1023t identified for organics for which adsorption is not favored. We may accordingly conclude that apart from the high crystallinity of the anatase nanocrystals, the photocatalytic activity of ECT-1023t is further augmented by the enhanced charge separation efficiency due to the rutile-anatase electron transfer along with the higher propensity of the catalyst to generate highly reactive hydroxyl radicals in comparison with the P25 mixed phase photocatalyst.

4. Conclusions

The evolution of structure and microstructure as well as charge separation for a series of highly reactive nanocrystalline TiO_2 photocatalysts, certified by the degradation-mineralization of various model pollutants under UV light, were comparatively investigated to the benchmark Aeroxide® P25 photocatalyst by powder XRD, Raman and light-induced EPR spectroscopy in order to determine the key parameters underlying the phase and size dependence of their distinct photocatalytic performance for water detoxification. For the smallest single phase anatase nanoparticles, Rietveld refinement and W-H plot analyses consistently revealed the development of anisotropic microstrains accompanied by lattice contraction relative to the bulk phase, mainly due to the shortening of the *c*-axis and the weak elongation of the *a*-axis. Increase of the calcination temperature resulted in particle growth and relaxation of both lattice deformation and anisotropic microstrains. The size dependence of microstrain values scaled linearly with the relative change of the *c*-axis lattice parameter and the broadening of the main anatase Raman mode, indicating an inherent correlation between lattice deformation and microstrains for the anatase nanoparticles. Calcination at 1023 K resulted in the formation of an anatase (82%)/rutile(18%) mixed phase TiO_2 nanomaterial with optimal photocatalytic performance, exceeding that of P25 over a wide range of organic water pollutants. This highly efficient photocatalyst comprised anatase nanocrystals essentially "free" from lattice deformation and microstrains, as well as larger, yet strained, rutile nanocrystals compared to those of P25, for which an additional electron trapping lattice site was identified by light-induced EPR spectroscopy. More importantly, electron transfer from the rutile to the anatase lattice trap states was derived by comparative EPR measurements under visible light, likewise charge transfer via trapping sites originally proposed by Hurum

et al. for P25. The favorable combination of high crystal quality for the anatase nanocrystals (major active phase) with the rutile-to-anatase electron transfer in the case of interfacial coupling can be thus concluded to reduce electron-hole recombination and boost the photocatalytic activity of the sol-gel mixed phase material in comparison with the P25 photocatalyst. Improvement of the anatase nanoparticle crystal quality even at the expense of surface area and interfacial coupling to rutile nanoparticles are key to the design and engineering of mixed phase titania for solar light photocatalytic applications.

Acknowledgements

Appendix A. Supplementary data

Supplementary data associated with this article can be found, in the online version, at http://dx.doi.org/10.1016/j.apcatb.2016.03.068.

References

[1] A. Fujishima, X. Zhang, D.A. Tryk, Surf. Sci. Rep. 63 (2008) 515–582.
[2] Y. Ma, X. Wang, Y. Jia, X. Chen, H. Han, C. Li, Chem. Rev. 114 (2014) 9987–10043.
[3] X. Chen, A. Selloni, Chem. Rev. 114 (2014) 9281–9282.
[4] A.V. Emeline, X. Zhang, M. Jin, T. Murakami, A. Fujishima, J. Phys. Chem. B 110 (2006) 7409–7413.
[5] M. Pelaez, N.T. Nolan, S.C. Pillai, M.K. Seery, P. Falaras, A.G. Kontos, P.S.M. Dunlop, J.W.J. Hamilton, J.A. Byrne, K. O'shea, M.H. Entezari, D.D. Dionysiou, Appl. Catal. B 125 (2012) 331–349.
[6] A. Kubacka, M. Fernandez-García, G. Colon, Chem. Rev. 112 (2012) 1555–1614.
[7] R. Asahi, T. Morikawa, H. Irie, T. Ohwaki, Chem. Rev. 114 (2014) 9824–9852.
[8] S. Banerjee, S.C. Pillai, P. Falaras, K.E. O'shea, J.A. Byrne, D.D. Dionysiou, J. Phys. Chem. Lett. 5 (2014) 2543–2554.
[9] X. Zhang, Y.L. Chen, R.-S. Liu, D.P. Tsai, Rep. Prog. Phys. 76 (2013) 046401.
[10] H. Zhang, G. Chen, D.W. Bahnemann, J. Mater. Chem. 19 (2009) 5089–5121.
[11] H. Tada, J. Jin, A. Iwaszuk, M. Nolan, J. Phys. Chem. C 118 (2014) 12077–12086.
[12] L.M. Pastrana-Martínez, S. Morales-Torres, V. Likodimos, J.L. Figueiredo, J.L. Faria, P. Falaras, A.M.T. Silva, Appl. Catal. B 123–124 (2012) 241–256.
[13] S.M. Miranda, G.E. Romanos, V. Likodimos, R.R.N. Marques, E.P. Favvas, F.K. Katsaros, K.L. Stefanopoulos, V.J.P. Vilar, J.L. Faria, P. Falaras, A.M.T. Silva, Appl. Catal. B 147 (2014) 65–81.
[14] L. Liu, X. Chen, Chem. Rev. 114 (2014) 9890–9918.
[15] G.H. Li, K.A. Gray, Chem. Phys. 339 (2007) 173–187.
[16] X. Chen, L. Liu, P.Y. Yu, S.S. Mao, Science 331 (2011) 746–750.
[17] J. Tao, T. Luttrell, M. Batzill, Nat. Chem. 3 (2011) 296–300.
[18] H.G. Yang, C.H. Sun, S.Z. Qiao, J. Zou, G. Liu, S.C. Smith, H.M. Cheng, G.Q. Lu, Nature 453 (2008) 638–641.
[19] V. Likodimos, C. Han, M. Pelaez, A.G. Kontos, G. Liu, D. Zhu, S. Liao, A.A. de la Cruz, K. O'shea, P.S.M. Dunlop, J.A. Byrne, D.D. Dionysiou, P. Falaras, Ind. Eng. Chem. Res. 52 (2013) 13957–13964.
[20] M. Batzill, Energy Environ. Sci. 4 (2011) 3275–3286.
[21] H. Irie, Y. Watanabe, K. Hashimoto, J. Phys. Chem. B 107 (2003) 5483–5486.
[22] G. Barolo, S. Livraghi, M. Chiesa, M.C. Paganini, E. Giamello, J. Phys. Chem. C 116 (2012) 20887–20894.
[23] L.M. Pastrana-Martinez, S. Morales-Torres, A.G. Kontos, N.G. Moustakas, J.L. Faria, J.M. Dona-Rodriguez, P. Falaras, A.M.T. Silva, Chem. Eng. J. 224 (2013) 17–23.
[24] H. Zhang, J.F. Banfield, J. Phys. Chem. B 104 (2000) 3481–3487.
[25] O.-O. Prieto-Mahaney, N. Murakami, R. Abe, B. Ohtani, Chem. Lett. 38 (2009) 238–239.
[26] M. Xu, Y. Gao, E.M. Moreno, M. Kunst, M. Muhler, Y. Wang, H. Idriss, C. Wöll, Phys. Rev. Lett. 106 (2011) 138302.
[27] T. Luttrell, S. Halpegamage, J. Tao, A. Kramer, E. Sutter, M. Batzill, Sci. Rep. 4 (2014) 4043.
[28] Q. Sun, Y. Xu, J. Phys. Chem. C 114 (2010) 18911–18918.
[29] A. Li, R. Liu, Y. Xu, J. Phys. Chem. C 117 (2013) 24360–24367.
[30] Z. Li, S. Cong, Y. Xu, ACS Catal. 4 (2014) 3273–3280.
[31] J.T. Carneiro, T.J. Savenije, J.A. Mouljin, G. Mul, J. Phys. Chem. C 114 (2010) 327–332.
[32] J.T. Carneiro, T.J. Savenije, J.A. Mouljin, G. Mul, J. Phys. Chem. C 115 (2011) 2211–2217.
[33] A.G. Agrios, P. Pichat, J. Photochem. Photobiol. A 180 (2006) 130–135.
[34] M. Inagaki, R. Nonaka, B. Tryba, A.W. Morawski, Chemosphere 64 (2006) 437–445.
[35] B. Tryba, M. Toyoda, A.W. Morawski, R. Nonaka, M. Inagaki, Appl. Catal. B 71 (2007) 163–168.
[36] M. Kong, Y. Li, X. Chen, T. Tian, P. Fang, F. Zheng, X. Zhao, J. Am. Chem. Soc. 133 (2011) 16414–16417.
[37] J. Ryu, W. Choi, Environ. Sci. Technol. 42 (2008) 294–300.
[38] C. Fernández-Rodríguez, J.M. Doña-Rodríguez, O. González-Díaz, I. Seck, D. Zerbani, D. Portillo, J. Perez-Peñna, Appl. Catal. B 125 (2012) 383–389.
[39] H. Zhang, J.F. Banfield, Chem. Rev. 114 (2014) 9613–9644.
[40] T. Ohno, K. Sarukawa, K. Tokieda, M. Matsumura, J. Catal. 203 (2001) 82–86.
[41] D.C. Hurum, A.G. Agrios, K.A. Gray, T. Rajh, M.C. Thurnauer, J. Phys. Chem. B 107 (2003) 4545–4549.
[42] D.C. Hurum, K.A. Gray, T. Rajh, M.C. Thurnauer, J. Phys. Chem. B 109 (2005) 977–980.
[43] R.I. Bickley, T. Gonzalez-Carreno, J.S. Lees, L. Palmisano, R.J. Tilley, J. Solid State Chem. 92 (1991) 178–190.
[44] P. Deaík, B. Aradi, T. Frauenheim, J. Phys. Chem. C 115 (2011) 3443–3446.
[45] D.O. Scanlon, C.W. Dunnill, J. Buckeridge, S.A. Shevlin, A.J. Logsdail, S.M. Woodley, C.R.A. Catlow, M.J. Powell, R.G. Palgrave, I.P. Parkin, G.W. Watson, T.W. Keal, P. Sherwood, A. Walsh, A.A. Sokol, Nat. Mater. 12 (2013) 798–801.
[46] V. Pfeifer, P. Erhart, S. Li, K. Rachut, J. Morasch, J. Broetz, P. Reckers, T. Mayer, S. Ruehle, A. Zaban, I. Mora-Seró, J. Bisquert, W. Jaegermann, A. Klein, J. Phys. Chem. Lett. 4 (2013) 4182–4187.
[47] S. Cong, Y. Xu, J. Phys. Chem. C 115 (2011) 21161–21168.
[48] T. Xia, N. Li, Y.L. Zhang, M.B. Kruger, J. Murowchick, A. Selloni, X. Chen, ACS Appl. Mater. Interfaces 5 (2013) 9883–9890.
[49] S. Shen, X. Wang, T. Chen, Z. Feng, C. Li, J. Phys. Chem. C 118 (2014) 12661–12668.
[50] M.-G. Ju, G. Sun, J. Wang, Q. Meng, W.Z. Liang, ACS Appl. Mater. Interfaces 6 (2014) 12885–12892.
[51] J.C. Garcia, M. Nolan, N.A. Deskins, J. Chem. Phys. 142 (2015) 024708.
[52] Y. Mi, Y. Weng, Sci. Rep. 5 (2015) 11482.
[53] J. Aran~a, J.M. Don~a-Rodriguez, D. Portillo-Carrizo, C. Fernandez-Rodriguez, J. Perez-Pen~a, O. Gonzalez-Diaz, J.A. Navio, M. Macias, Appl. Catal. B 100 (2010) 346–354.
[54] E.I. Seck, J.M. Doña-Rodríguez, C. Fernández-Rodríguez, O.M. González-Díaz, J. Araña, J. Pérez-Peña, Appl. Catal. B 125 (2012) 28–34.
[55] E.I. Seck, J.M. Doña-Rodríguez, C. Fernández-Rodríguez, O.M. González-Díaz, J. Araña, J. Pérez-Peña, Chem. Eng. J. 203 (2012) 52–62.
[56] V. Maroga Mboula, V. Héquet, Y. Andrès, L.M. Pastrana-Martínez, J.M. Doña-Rodríguez, A.M.T. Silva, P. Falaras, Water Res. 47 (2013) 3997–4005.
[57] V. Maroga Mboula, V. Héquet, Y. Andrès, Y. Gru, R. Colin, J.M. Doña-Rodríguez, L.M. Pastrana-Martínez, A.M.T. Silva, M. Leleu, A.J. Tindall, S. Mateos, P. Falaras, Appl. Catal. B 162 (2015) 437–444.
[58] L.M. Pastrana-Martinez, J.L. Faria, J.M. Doña-Rodríguez, C. Fernández-Rodríguez, A.M.T. Silva, Appl. Catal. B 113–114 (2012) 221–227.
[59] E.I. Seck, J.M. Doña-Rodríguez, C. Fernández-Rodríguez, D. Portillo-Carrizo, M.J. Hernández-Rodríguez, O.M. González-Díaz, J. Pérez-Peña, Sol. Energy 87 (2013) 150–157.
[60] J. Rodríguez-Carvajal, Physica B 192 (1993) 55–69.
[61] M. Horn, C.F. Schwerdtfeger, E.P. Meagher, Zeitschrift für. Kristallographie 136 (1972) 273–281.
[62] C.J. Howard, Z.M. Sabine, F. Dickson, Acta Cryst. B 47 (1991) 462–468.
[63] G. Zahariou, N. Ioannidis, G. Sioros, V. Petrouleas, Biochemistry 46 (2007) 14335–14341.
[64] D.E. Santiago, J.M. Dona-Rodriguez, J. Arana, C. Fernandez-Rodriguez, O. Gonzalez-Diaz, J. Perez-Pena, A.M.T. Silva, Appl. Catal. B 138-139 (2013) 391–400.
[65] G.S. Li, L.P. Li, J. Boerio-Goates, B.F. Woodfield, J. Am. Chem. Soc. 127 (2005) 8659–8666.
[66] I. Djerdj, A.M. Tonejc, J. Alloys Compd. 413 (2006) 159–174.
[67] V. Swamy, D. Menzies, B.C. Muddle, A. Kuznetsov, L.S. Dubrovinsky, Q. Dai, V. Dmitriev, Appl. Phys. Lett. 88 (2006) 243103.
[68] G. Colón, M.C. Hidalgo, G. Munuera, I. Ferino, M.C. Cutrufello, M.A. Navío, Appl. Catal. B 63 (2006) 45–59.
[69] I.E. Grey, N.C. Wilson, J. Solid State Chem. 180 (2007) 670–678.
[70] H. Zhang, B. Chen, J.F. Banfield, Phys. Chem. Chem. Phys. 11 (2009) 2553–2558.
[71] S. Vives, C. Meunier, Powder Diffr. 24 (2009) 205–220.
[72] G.V. Jensen, M. Bremholm, N. Lock, G.R. Deen, T.R. Jensen, B.B. Iversen, M. Niederberger, J.S. Pedersen, H. Birkedal, Chem. Mater. 22 (2010) 6044–6055.
[73] J.K. Burdett, T. Hughbanks, G.J. Miller, J.W. Richardson, J.V. Smith, J. Am. Chem. Soc. 109 (1987) 3639–3646.
[74] V. Swamy, A.Y. Kuznetsov, L.S. Dubrovinsky, A. Kurnosov, V.B. Prakapenka, Phys. Rev. Lett. 103 (2009) 075505.
[75] AEROXIDE®, AERODISP®, AEROPERL®, Titanium Dioxide as Photocatalyst, Technical Information 1243, Evonik Industries, http://oil-additives.evonik.

com/sites/lists/IM/Documents/TI-1243-Titanium-Dioxide-as-Photocatalyst-EN.pdf.

[76] E.J. Mittemeijer, U. Welzel, Zeitschrift für. Kristallographie 223 (2008) 552–560.

[77] W. Qin, T. Nagase, Y. Umakoshi, J.A. Szpunar, Phil. Mag. Lett. 88 (2008) 169–179.

[78] U. Balachandran, N.G. Eror, J. Solid State Chem. 42 (1982) 276–282.

[79] J. Zhang, M. Li, Z. Feng, J. Chen, C. Li, J. Phys. Chem. B 110 (2006) 927–935.

[80] S. Kelly, F.H. Pollak, M. Tomkiewicz, J. Phys. Chem. B 101 (1997) 2730–2734.

[81] V. Likodimos, T. Stergiopoulos, P. Falaras, J. Kunze, P. Schmuki, J. Phys. Chem. C 112 (2008) 12687–12696.

[82] E. Nakaoka, Z. Nosaka, J. Photochem. Photobiol. A 110 (1997) 299–305.

[83] J.M. Coronado, A.J. Maira, J.C. Conesa, K.L. Yeung, V. Augugliaro, J. Soria, Langmuir 17 (2001) 5368–5374.

[84] T. Berger, M. Sterrer, O. Diwald, E. Knozinger, ChemPhysChem 6 (2005) 2104–2112.

[85] E. Carter, A.F. Carley, D.M. Murphy, J. Phys. Chem. C 111 (2007) 10630.

[86] T. Berger, M. Sterrer, O. Diwald, E. Knozinger, D. Panayotov, T.L. Thompson, J.T. Yates Jr., J. Phys. Chem. B 109 (2005) 6061–6068.

[87] C.P. Kumar, N.O. Gopal, T.C. Wang, M.S. Wong, S.C. Ke, J. Phys. Chem. B 110 (2006) 5223–5229.

[88] G. Li, N.M. Dimitrijevic, L. Chen, J.M. Nichols, T. Rajh, K.A. Gray, J. Am. Chem. Soc. 130 (2008) 5402–5403.

[89] H.-H. Lo, N.O. Gopal, S.-C. Sheu, S.-C. Ke, J. Phys. Chem. C 118 (2014) 2877–2884.

[90] C. Di Valentin, A. Selloni, J. Phys. Chem. Lett. 2 (2011) 2223–2228.

[91] T. Hirakawa, K. Yawata, Y. Nosaka, Appl.Catal. A 325 (2007) 105–111.